### Title
Dynamics and mass balance of Taylor Glacier, Antarctica: 1. Geometry and surface velocities




### Journal
Journal of Geophysical Research, 114(F4)

### ISSN
0148-0227



### Authors
Kavanaugh, JL
Cuffey, KM
Morse, DL
et al.



### Publication Date
2009

### DOI
10.1029/2009jf001309

# Dynamics and mass balance of Taylor Glacier, Antarctica: 1. Geometry and surface velocities

J. L. Kavanaugh,[1] K. M. Cuffey,[2] D. L. Morse,[3] H. Conway,[4] and E. Rignot[5]

Received 15 March 2009; revised 14 June 2009; accepted 7 July 2009; published 3 November 2009.

[1] Taylor Glacier, Antarctica, exemplifies a little-studied type of outlet glacier, one that flows slowly through a region of rugged topography and dry climate. This glacier, in addition, connects the East Antarctic Ice Sheet with the McMurdo Dry Valleys, a region much studied for geomorphology, paleoclimate, and ecology. Here we report extensive new measurements of surface velocities, ice thicknesses, and surface elevations, acquired with InSAR, GPS, and GPR. The latter two were used to construct elevation models of the glacier's surface and bed. Ice velocities in 2002–2004 closely matched those in 2000 and the mid-1970s, indicating negligible interannual variations of flow. Comparing velocities with bed elevations shows that, along much of the glacier, flow concentrates in a narrow axis of relatively fast flowing ice that overlies a bedrock trough. The flow of the glacier over major undulations in its bed can be regarded as a "cascade"; it speeds up over bedrock highs and through valley narrows and slows down over deep basins and in wide spots. This pattern is an expected consequence of mass conservation for a glacier near steady state. Neither theory nor data from this Taylor Glacier study support the alternative view, recently proposed, that an outlet glacier of this type trickles slowly over bedrock highs and flows fastest over deep basins.

**Citation:** Kavanaugh, J. L., K. M. Cuffey, D. L. Morse, H. Conway, and E. Rignot (2009), Dynamics and mass balance of Taylor Glacier, Antarctica: 1. Geometry and surface velocities, *J. Geophys. Res.*, *114*, F04010, doi:10.1029/2009JF001309.

## 1. Introduction

[2] Taylor Glacier is an outlet of the East Antarctic Ice Sheet. It originates on Taylor Dome, a local flow center, and descends eastward through the Transantarctic Range to terminate in Taylor Valley, the southernmost of the famous McMurdo Dry Valleys of Victoria Land (Figure 1). Sidelobes of Taylor Glacier terminate in ice-free tributary valleys. Ice flows into Taylor Glacier from both Cassidy and Ferrar glaciers, with the latter contributing ice in two locations, Windy Gully and the Taylor-Ferrar confluence.

[3] Building on efforts of earlier researchers (in particular, *Robinson* [1984]), we have undertaken a comprehensive study of the ice dynamics in Taylor Glacier's ~80-km-long ablation zone. This paper, the first in a series of three, describes the modern geometrical configuration and flow of Taylor Glacier. The second paper reports on the force balance and longitudinal coupling of the glacier [*Kavanaugh and Cuffey*, 2009], and the third examines the along-flow pattern of ice flux and the state of mass balance [*Kavanaugh et al.*, 2009]. Results from a survey of the along-flow variation of ice isotopes were presented by *Aciego et al.* [2007]. Dynamics of the accumulation zone on Taylor Dome were studied as part of the earlier Taylor Dome project [*Steig et al.*, 2000; *Grootes et al.*, 2001; *Morse et al.*, 1998, 1999, 2007].

### 1.1. Motivations

[4] Characterizing the flow and configuration of Taylor Glacier is important for the following reasons:

[5] 1. Taylor Glacier offers a unique opportunity to study an Antarctic glacial system for which specific, though incomplete, information is available about both forcings and responses. Taylor Dome, the source of Taylor Glacier, is the site of an ice core paleoclimate record of greater than 100 ka duration [*Steig et al.*, 2000; *Monnin et al.*, 2004]. In addition, lower Taylor Valley and the ice-free tributary valleys contain a glacial geologic record of past ice incursions. These have also been studied extensively [e.g., *Hendy et al.*, 1979; *Denton et al.*, 1989, 1993; *Brook et al.*, 1993; *Marchant et al.*, 1993; *Higgins et al.*, 2000]. The geologic evidence indicates that Taylor Glacier and smaller alpine glaciers in the region expand during interglacial periods and recede during glacial ones, a behavior that is antiphased with that of the whole Antarctic Ice Sheet [*Higgins et al.*, 2000]. Thus, whereas the whole ice sheet responds primarily to changes of sea level and ocean temperature, Taylor Glacier responds to local factors. The waxing and

[1]Department of Earth and Atmospheric Sciences, University of Alberta, Edmonton, Alberta, Canada.
[2]Department of Geography, University of California, Berkeley, California, USA.
[3]Institute for Geophysics, University of Texas at Austin, Austin, Texas, USA.
[4]Department of Earth and Space Sciences, University of Washington, Seattle, Washington, USA.
[5]Department of Earth System Science, University of California, Irvine, California, USA.


0148-0227/09/2009JF001309

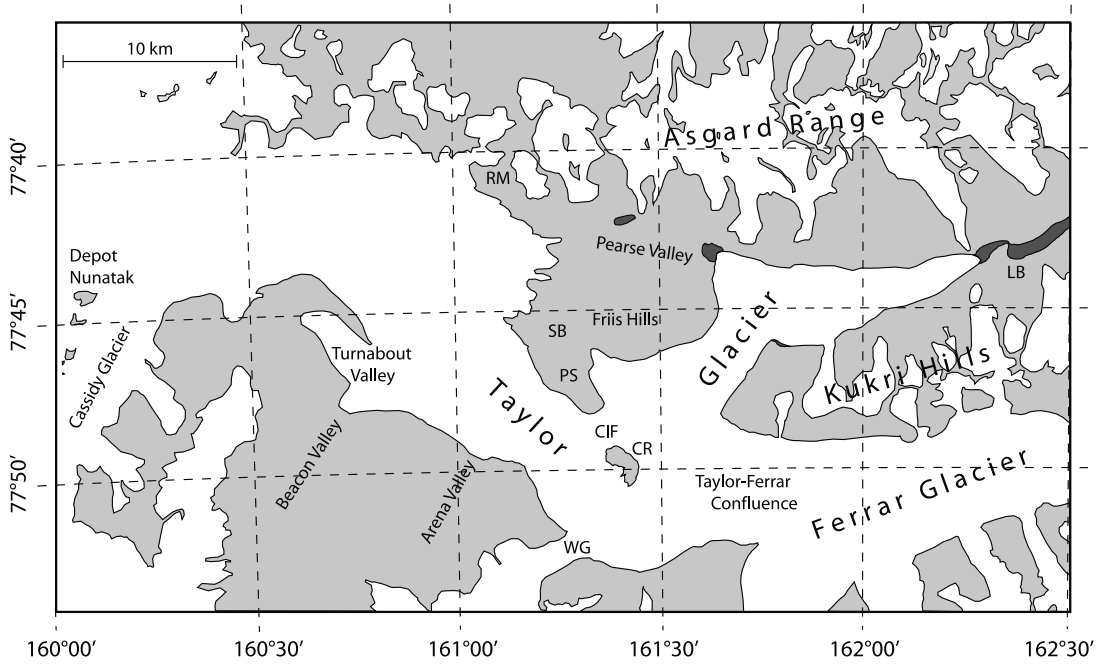


**Figure 1.** Map view of Taylor Glacier region. Abbreviations are Round Mountain (RM), Simmons Basin (SB), Pandora Spire (PS), the Cavendish Ice Falls (CIF), Cavendish Rocks (CR), Windy Gully (WG), and Lake Bonney (LB).

waning of Taylor Glacier might indicate accumulation rate and thickness changes in the nearby sector of the East Antarctic Ice Sheet.

[6] 2. Taylor Glacier is a major physical influence on the Taylor Valley environment, which is the best studied ice-free region of Antarctica and a Long Term Ecological Research Network site [e.g., *Fountain et al.*, 1999; *Lyons et al.*, 2000; *Doran et al.*, 2002]. Taylor Glacier defines the western boundary of the ice-free region. Geologic evidence shows that Taylor Glacier expanded more than 10 km eastward into this valley between 70 and 130 ka ago [*Higgins et al.*, 2000]. Understanding the dynamics of the glacier will be needed for understanding past incursions into Taylor Valley and tributary valleys.

[7] 3. The lower ablation zone of Taylor Glacier might prove to be a valuable "ice mine" for paleoclimate studies. *Aciego et al.* [2007] have shown that ice from the last glacial period and its termination are exposed over more than 10 km along the central flow line. Here, large-volume samples can be extracted in order to measure rare constituents, including trace gases and microparticles, and the isotopic compositions of both. In this context, it is important to understand how the ice was conveyed from the accumulation zone to its current sites of outcrop. For this reason, the velocity field of the glacier must be known.

[8] 4. Taylor Glacier exemplifies an ice sheet outlet originating on a local dome and flowing through a rugged mountainous landscape. The ice thickness varies significantly along the glacier as it enters deep basins and flows over bedrock ribs. The flow is sluggish, of order 10 m $a^{-1}$, despite a typical glaciologic driving stress, of order 100 kPa [*Kavanaugh and Cuffey*, 2009]. High-stress but slow flowing outlet glaciers do not contribute much to the overall transport of ice off the Antarctic continent. They are very interesting, nonetheless, because they are abundant features along some sectors of the ice sheet margin, like Victoria Land, and have received little attention.

### 1.2. Prior Work

[9] The first major analysis of Taylor Glacier dynamics was that of *Robinson* [1984], based on work at the glacier from 1975–1978. Compared to this earlier investigation, our study increases the spatial coverage, conceptual scope, and accuracy of analyses. Some of the techniques we used for data acquisition were not available in the 1970s. The accuracy of the earlier measurements of ice velocity, based on optical surveys, was not high; repeat surveys showed irregular interannual variations of flow that are unlikely to be real [*Robinson*, 1984, Figure 3]. A more significant limitation of the earlier study is that ice thicknesses were not well known. In addition, Robinson acquired no information about surface mass balances or ice fluxes above elevations of about 1.1 km. Here we extend measurements to ~1.7 km elevation, spanning the entire ablation zone.

[10] *Hubbard et al.* [2004] examined the lowest 8 km of Taylor Glacier. They constructed a detailed map of bed elevations using radar surveys, and performed a coupled heat and ice flow analysis to infer basal temperatures. The surveys showed that this lower end of the glacier sits in a U-shaped trough, overdeepened by about 100 m with respect to the terminus. Strong reflections from the bed indicated the presence of water in the deepest regions. Estimated basal temperatures, however, did not exceed −7 to −8°C; the water is most likely hypersaline. Compared to the work of *Hubbard et al.* [2004], our study examines a much larger portion of the glacier, but at a lower spatial

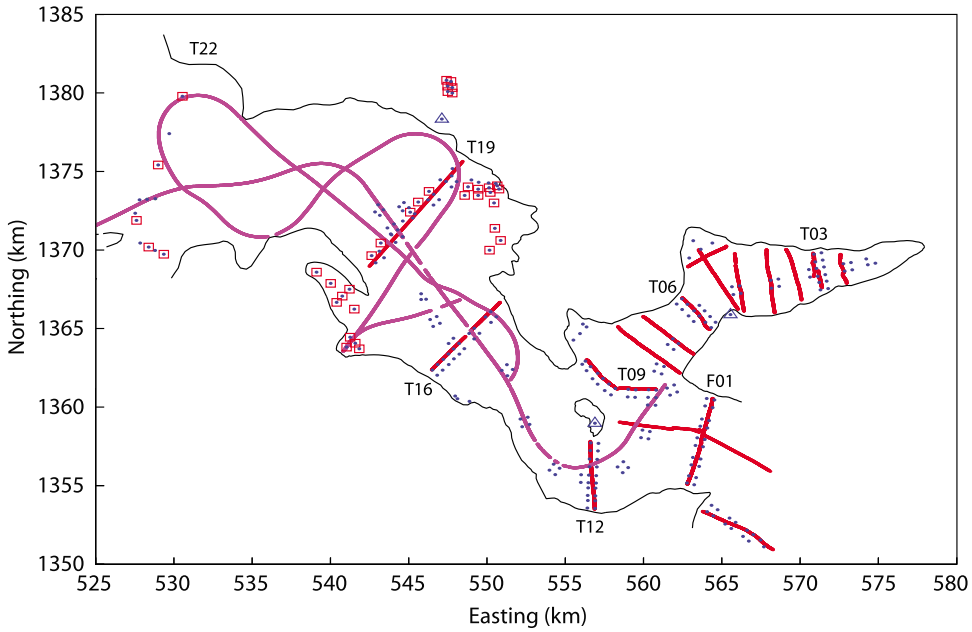


**Figure 2.** Map view of survey marker locations (blue dots), GPS "base stations" (blue triangles), ground-based radar survey transects (red lines) and spot measurements (red squares), and airborne radar survey transects (magenta lines). Labels with "T" and "F" refer to sites on Taylor and Ferrar glaciers, respectively.

resolution. Our results concerning basal temperatures are reported by *Kavanaugh and Cuffey* [2009].

### 1.3. Cascade and Trickle Models

[11] Recently, *Johnson and Staiger* [2007] proposed a model for polar outlet glaciers flowing slowly through mountainous landscapes. Their view was constructed from a numerical analysis of Ferrar Glacier, Taylor Glacier's neighbor to the south. The model simulated flow and forces along a flow line, using a finite element technique that accounted for higher-order stresses. Ice thicknesses along the flow line were taken from airborne radar soundings reported by *Calkin* [1974], consisting of a single flight path that attempted to follow the glacier centerline. The authors concluded that the slowest flow, with rates of less than 1 m $a^{-1}$, occurs in thin-ice regions overlying subglacial summits, and the fastest flow in deep basins. Their calculated surface velocities fluctuate by an order of magnitude over distances of 10 km along the flow line. They concluded that "curious flow patterns arise in the glacier" and described the glacier as "trickling" over mountain ranges; we will refer to this hypothesis as the "trickle" model. The model of *Johnson and Staiger* [2007] was not compared to any velocity data.

[12] Superficially, this view of outlet glacier dynamics seems implausible. It implies large rates of longitudinal extension and compression that induce an alternating pattern of upward and downward vertical velocities at the glacier surface (unless the width varies dramatically; the Johnson and Staiger analysis specifically assumed that width varies little, however). For the glacier to resemble a steady configuration, this pattern requires an alternation of accumulation and ablation at the surface in order to conserve mass. Such patterns are rarely, if ever, observed. It is much more likely that ablation varies slowly along the surface and, in order to conserve mass, the glacier flows faster through thin regions, with faster flow driven by increased surface slopes and driving stresses. This second model describes the same pattern seen in a cascading river and so we call it the "cascade" model. Because the bed of Taylor Glacier undulates in a fashion similar to that beneath Ferrar [*Calkin*, 1974, Figure 5], Taylor Glacier provides a test of these views.

### 1.4. Goals of This Paper

[13] This paper elucidates the main features of surface velocity, ice thickness, and bed topography of Taylor Glacier. We discuss the form of the glacier's bed and speculate about factors influencing its erosional development. We assess the merits of the trickle and cascade conceptions of ice sheet outlet flow. In addition, this paper outlines a method, perhaps useful elsewhere, for generating a map of subglacial valley form using scattered measurements of ice thickness.

[14] We first summarize our newly acquired measurements of surface velocity and ice thickness and then present the elevation models. Appendices A and B contain details of the model generation methods.

## 2. New Data Acquired

### 2.1. Survey Network

[15] In austral summer 2002–2003, we constructed a network of 265 survey markers (Figure 2). Of these, 221 were installed in Taylor Glacier, 14 in Ferrar Glacier, 20 in the confluence of Ferrar and Taylor glaciers, 4 in Cassidy Glacier, and 6 in a nearby unnamed cirque glacier in

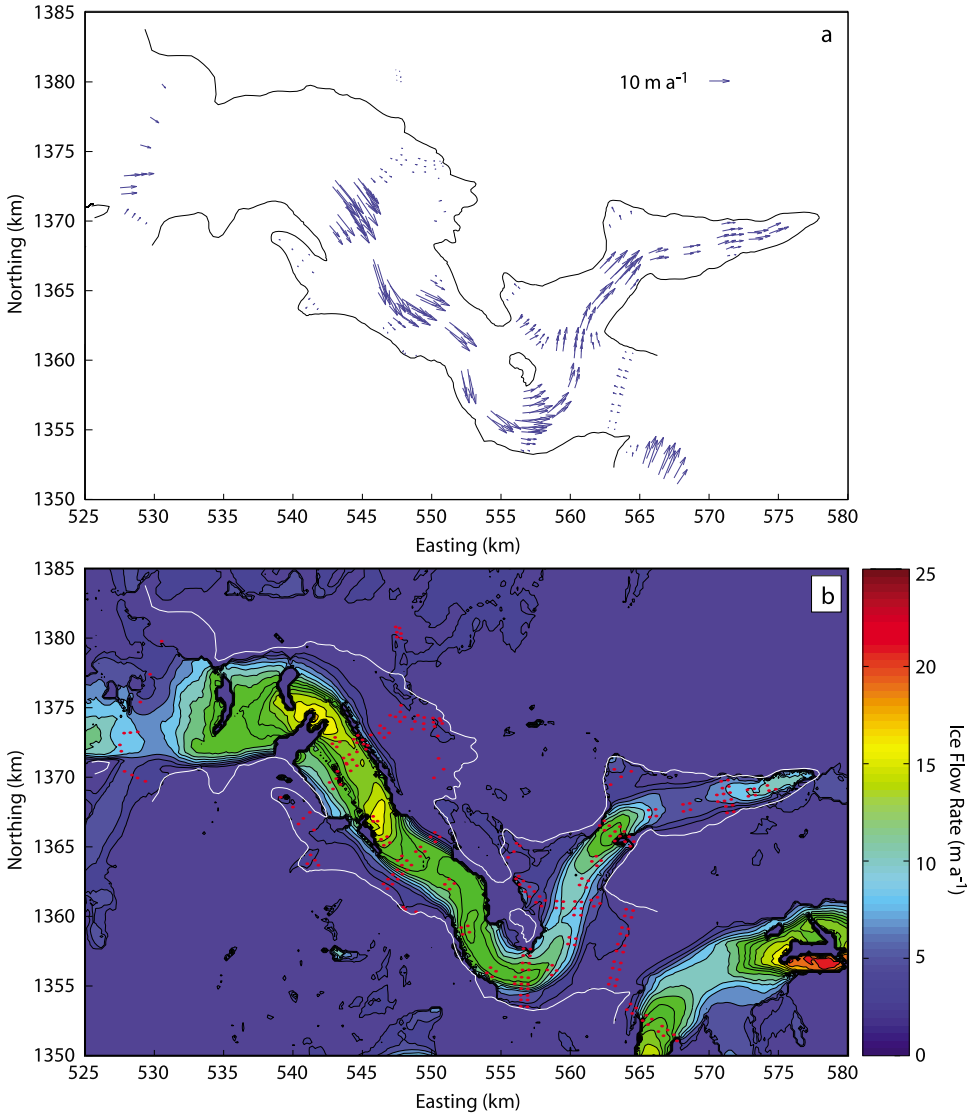


**Figure 3.** Taylor Glacier surface flow velocities. (a) Point velocities determined from repeat GPS survey. (b) Magnitudes of velocities obtained from InSAR (units m $a^{-1}$); regions of missing data are zones of rapid strain where aliasing precludes phase unwrapping. The white line indicates the glacier edge, and red dots are locations of survey poles.

the Asgard Range. The markers were 3.3-m-long poles of 1-inch diameter aluminum electrical conduit installed ~2 m into the ice. We also found eight survey poles remaining from studies at this site by E. Waddington and colleagues in the early 1990s. Further, we installed three monuments (hereafter "base stations") in off-ice locations in order to provide stable points of reference (Figure 2). These consisted of bolts drilled into bedrock (at base stations 2 and 3) and a large boulder on a moraine (base station 1).

[16] The markers we installed on the glacier were arranged in order to facilitate calculations of ice flux through valley cross sections and into tributary lobes, to measure ice strain rates and their gradients, and to measure surface mass balances over much of the glacier. Some regions of the glacier, especially in its upper section, were excluded from the survey grid because of crevasse hazards.

### 2.2. Velocities From Global Positioning System Surveys

[17] Positions of the survey markers were determined using GPS in austral summers of 2002–2003 and 2003–2004, and ice surface velocities were calculated from pole displacements during this interval. The GPS surveys used Trimble 5700 receivers operating in rapid static mode, and both L1 and L2 frequencies were recorded to apply ionospheric corrections. In order to calculate survey closure, a minimum of three GPS receivers were run simultaneously, with one receiver on an off-ice base station. Recording times were at least 20 minutes, but were extended when sky visibility or satellite coverage was limited. The position and velocity of each pole were calculated from these observations; both of these data sets (and their associated uncertainties) are available online from the National Snow and Ice Data Center [*Cuffey et al.*, 2007]. The mean 1.96$\sigma$

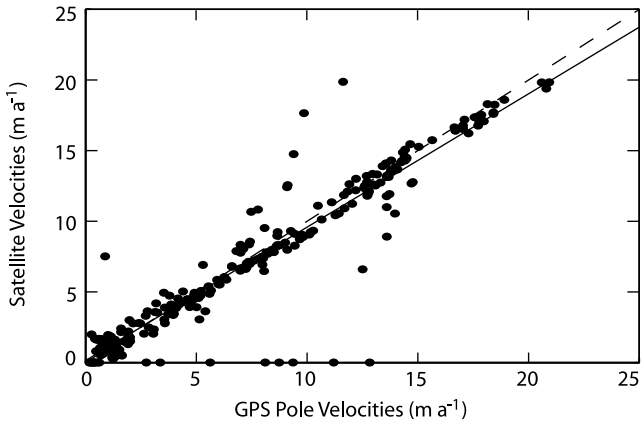


**Figure 4.** Comparison of ice surface velocities determined from repeat GPS survey (horizontal axis) and velocities at these locations obtained from radar satellite interferometry (vertical axis). Solid line represents the best fit least squares solution; dashed line represents 1:1 match.

(95% confidence) uncertainty in horizontal velocity was found to be 0.04 m $a^{-1}$, and the maximum uncertainty was 0.20 m $a^{-1}$.

[18] Figure 3a is a map of the measured flow vectors. The flow field includes a prominent bend around the Cavendish Rocks and a localized core of fast flow in the middle upper glacier.

[19] The highest rate of flow, 20.9 m $a^{-1}$, is 2 orders of magnitude slower than the fastest Antarctic ice streams. Ice enters the upper edge of the study region at 5–8 m $a^{-1}$. At their confluence, ice flows from Ferrar Glacier into Taylor Glacier at ~2 m $a^{-1}$, as previously observed by *Robinson* [1984]. Where the comparison can be made, our measured flow rates are close to those determined by Robinson from optical survey techniques (in the survey season declared by Robinson to be most accurate).

### 2.3. Velocities From Interferometry

[20] We have also determined glacier surface velocities by using satellite radar interferometric techniques. This provides a much more spatially complete view of the flow field than does the GPS survey network, although an assumption must be made about the small vertical component of flow.

[21] We used 24-day interferometric pairs of synthetic aperture radar (SAR) images from the Canadian Space Agency's Radarsat-1 instrument. The first pair, an ascending track, was acquired 21 September/15 October 2000. The second pair, a descending track, was acquired on the next orbit, only 1.6 h later. Each interferometric pair was unwrapped, georeferenced to a topographic model of the region provided by the U.S. Geological Survey (USGS), and coregistered. We obtained three-dimensional velocity vectors from the pair combination by assuming surface-parallel flow. The precision of mapping is a few centimeters per year if fringe noise is low, but degrades rapidly in areas of higher noise, to about 1–2 m $a^{-1}$. In a few parts of the glacier, where strain rates are large because the ice spills over bedrock ridges, we could not unwrap the phase due to aliasing.

[22] It is not possible, with Radarsat, to view the glacier in a third direction; thus emergence velocities cannot be determined. Typical emergence velocities should be similar to surface mass balances, hence of order 0.1 m $a^{-1}$, negligible compared to other velocity components.

[23] The 24-day repeat cycle of the Radarsat data used here is an unusual feature of our study. Such a long period would not work on most glaciers, because the surface decorrelates as it ages, and because aliasing of phases hides the full extent of deformation. However, the long interval is suitable at Taylor Glacier because the glacier's surface changes only slowly in the dry climate, and the glacier strains slowly.

[24] Figure 3b is a map of the velocity magnitudes determined with this method. The core stream of fast flow in the middle/upper glacier is an extensive and dominant feature. Its onset is about 10 km below the upper (western) edge of the study region.

[25] Overall agreement between satellite-derived and GPS-derived velocity magnitudes is very good (Figure 4). Least squares fitting of velocities from the two techniques gives a coefficient of determination $R^2 = 0.89$, while typical mismatches are about 1 m $a^{-1}$. The satellite-derived numbers tend to be unreliable, as a fraction of the GPS-measured velocity, only where the ice moves more slowly than about 5 m $a^{-1}$ and near the edges of the few heavily crevassed regions where the technique gave no results (blank regions on the glacier map in Figure 3b).

### 2.4. Ice Thickness From Ground Penetrating Radar Surveys

[26] Because the goals of this study required much better constraints on basal elevations than were previously available, we acquired new ice thickness data from ground penetrating radar (GPR) on ground traverses and airplane flights. Prior to these new measurements, the only available cross-sectional profiles along most of the glacier's length were generated from a gravity survey [*Robinson*, 1984], and the available airborne radar surveys were limited to longitudinal transects near the central axis of the glacier [*Calkin*, 1974; *Drewry*, 1982]. On valley glaciers like this one, side reflections and flight path meanders lead to large variations of apparent ice thickness which might bear no relation to actual changes in depth along the central flow line [e.g., *Holt et al.*, 2006b]. The cross-sectional valley form must also be constrained.

[27] On the lower 8 km of the glacier, *Hubbard et al.* [2004] made detailed surveys of ice thickness with a ground-based radar. For this region, ice thicknesses are already characterized in greater detail than provided by our new measurements.

#### 2.4.1. Ground-Based Surveys

[28] Using the University of Washington ±2 kV impulse radar system [*Gades*, 1998], we measured ice thickness along 16 across-glacier transects on Taylor Glacier, one transect across Ferrar Glacier, and one transect across the Taylor-Ferrar confluence (see Figure 2). Locations were obtained by pseudorange GPS. Reflection data were acquired at a center frequency of 7 MHz, and stacked (averaged) waveforms were recorded at 15 m intervals. Additional processing included band-pass filtering, corrections for surface topography, and migration. To convert

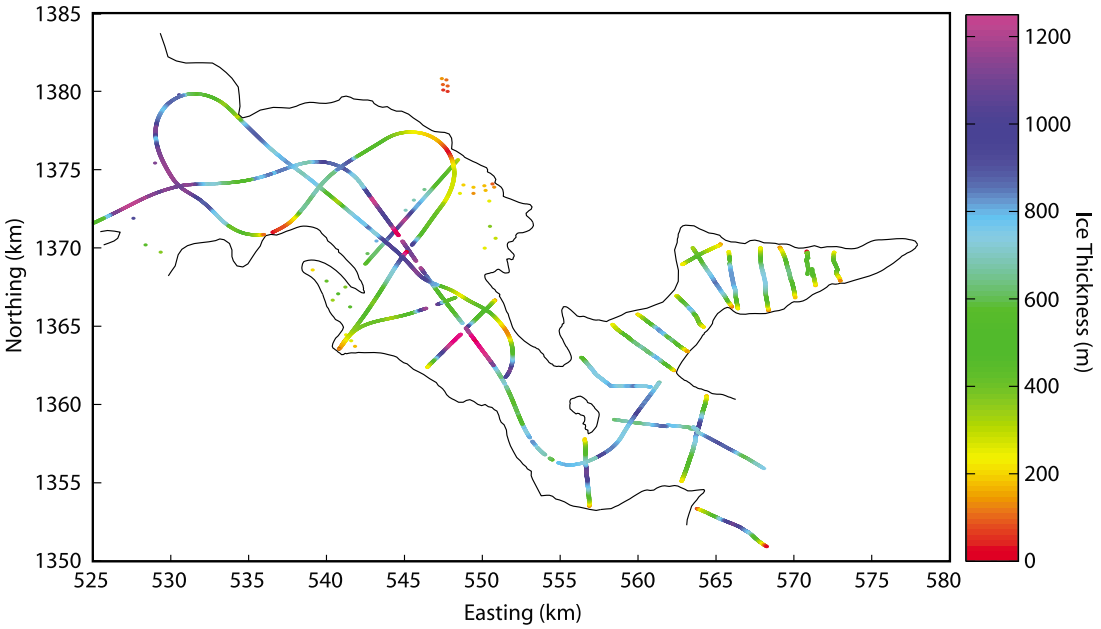


**Figure 5.** Map of measured ice thickness values (in m) obtained by ground-based and airborne GPR measurements.

two-way travel time to depth, we assumed wave speeds of 168.5 m $\mu s^{-1}$ in ice and 300.0 m $\mu s^{-1}$ in air. Most measurements were made in regions of bare ice, so no accounting for firn thickness was necessary. Uncertainty in depth estimates arises primarily from uncertainty in the wave speed in ice (about ±2 m $\mu s^{-1}$, corresponding to about 1.2% of the depth to a reflector), and from ambiguity in picking the travel time to the reflector (±0.01 $\mu$s, or about ±2 m). The resulting uncertainty is about ±10 m for an ice thickness of 700 m. Additional point measurements of ice thickness were obtained using the same system, at the locations indicated by red squares in Figure 2.

#### 2.4.2. Airborne Surveys

[29] In 2001 and 2004, the University of Texas Institute for Geophysics collected airborne radar sounding data for Taylor Glacier using the 7 kW, 60 MHz system described by *Holt et al.* [2006a] and *Peters et al.* [2005]; these references also describe the signal processing. Figure 2 shows the flight paths of the surveys.

#### 2.4.3. Ice Thickness Results

[30] Results of all the ice thickness measurements are shown together in Figure 5. The measurements with airborne instruments cannot be migrated, so ice thickness values do not exactly match at crossover points with other surveys. In general, however, the correspondence at crossover points is excellent. On the lower 8 km of the glacier, our measured ice thicknesses agree with those of *Hubbard et al.* [2004], to within uncertainties.

## 3. Glacier Geometry Model

[31] For some analyses, it is necessary to have a spatially continuous view of the glacier geometry. We have therefore constructed models for surface and bed elevations for the entire study region, using interpolation and data assimilation techniques. We emphasize that the analyses presented here (and especially by *Kavanaugh and Cuffey* [2009] and *Kavanaugh et al.* [2009]) use data only from regions where measurements of ice thickness and surface elevation are available. In these regions, the error in the elevation models is small; errors might be large, however, in sectors of the glacier that are far from sites of direct measurements.

### 3.1. Surface Elevation

[32] We are only interested in variations of surface elevation averaged over distances of about two ice thicknesses and greater; this is the length scale over which, according to theory, the compressive normal stress on horizontal planes in a glacier can be assumed equal to the weight of the ice overburden. As in most ice dynamical analyses, we will not consider variations at smaller scales [*Paterson*, 1994, p. 264]. Thus, the surface elevation model we constructed is for elevations averaged over a region of, typically, 1 to 2 km in diameter. Features of the glacier surface with smaller dimensions, like swales and longitudinal grooves, are not represented in the model. Near the glacier edges, where the ice is thin, we do not have enough information for an accurate model at the scale of two ice thicknesses.

[33] The foundation of our surface elevation map is the Radarsat Antarctic Mapping Project (RAMP) digital elevation model (DEM) Version 2 (resolution: 200 m) [*Liu et al.*, 2001]. There are systematic discrepancies between the RAMP model and the more accurate elevations determined by GPS on our survey grid. To incorporate these measurements, we first calculated a smoothed base map by convolving the RAMP model with a center-weighted filter of radius equal to max(800m, 2$H$), where $H$ is ice thickness. This initial smoothing minimized discrepancies between the base map and the GPS measurements of elevation. Most of these discrepancies were in the range −30 to +10 m (RAMP elevation minus GPS elevation). Since the discrepancies are

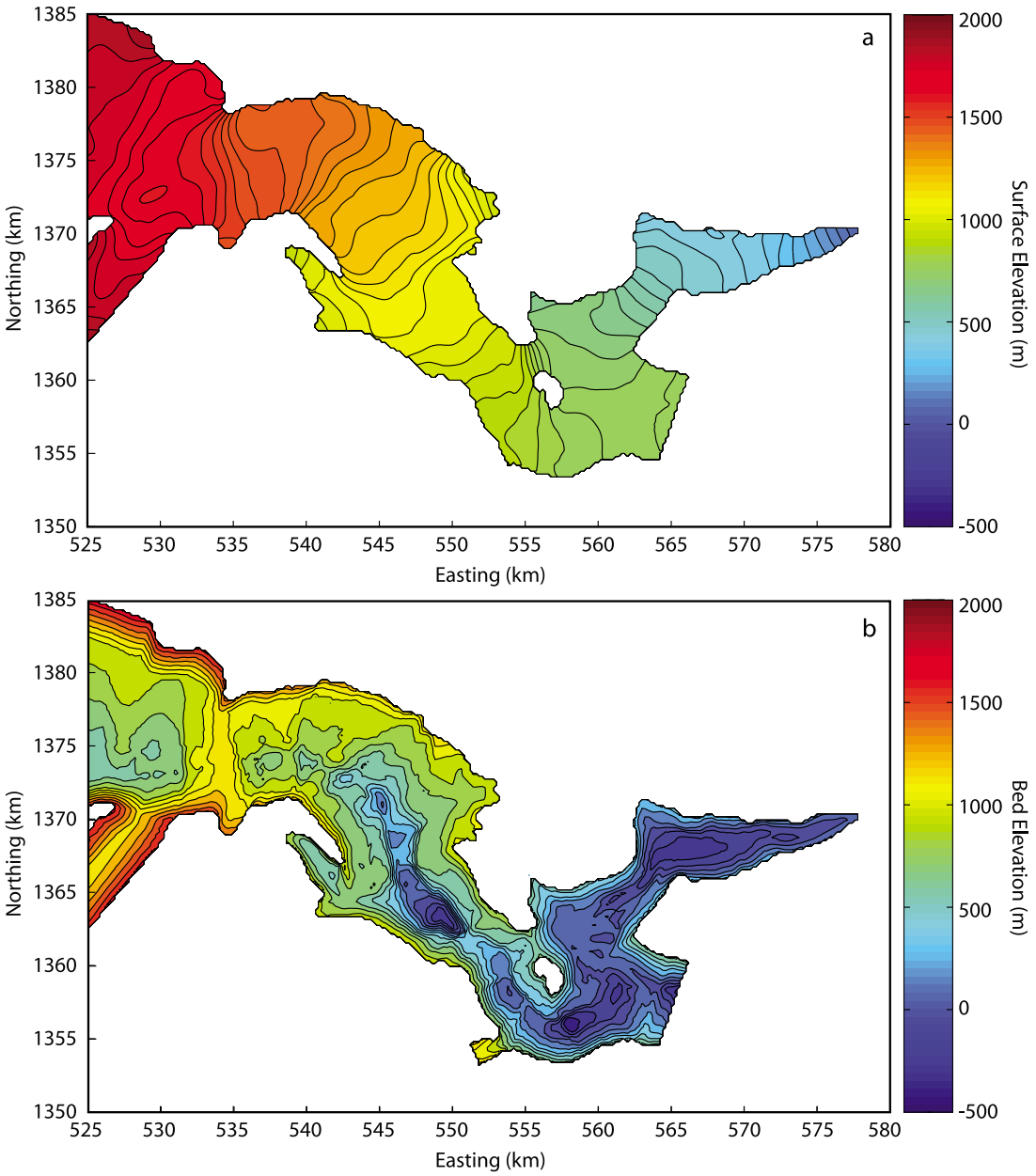


**Figure 6.** Elevation models (meters above sea level) for Taylor Glacier. (a) Surface digital elevation model, with 50 m contour interval. (b) Basal digital elevation model, with 125 m contour interval.

point values, corresponding to the survey network sites, it was necessary to construct an ''offset surface'' from them, a continuous surface covering the entire study region. To do so, every coordinate in the map was assigned an offset magnitude, equal to a weighted average of the measured discrepancies at nearby survey sites. The weighting was designed so that the closer survey sites had more influence than sites further away. The resulting offset surface was smoothed with a center-weighted filter of radius 1 km and then added to the elevation model. This produces a final model that closely matches the mean measured elevations in the vicinity of survey sites, is smooth at the scale of two ice thicknesses, and preserves all real features captured by the original RAMP model. Details of the method are given in Appendix A.

[34] Constructing the surface elevation model required some ad hoc choices about the shape and dimensions of filters. We believe the model is accurate for the following reasons. The corrections to the original RAMP model are very small compared to the entire range of elevations on the glacier. Moreover, the corrections were defined by our GPS measurements in such a way that the model must be accurate in the vicinity of the survey network sites. The elevation model shows all the features of the glacier surface that are apparent from field observations and USGS maps. On the other hand, near the glacier edges, where the ice is thin, the resolution of the elevation model is insufficient to show systematic variations at the scale of two ice thicknesses. Figure 6a shows the final surface DEM, which was used in all subsequent calculations.

### 3.2. Bed Elevation

[35] A bed elevation model was constructed by subtracting ice thicknesses from surface elevations. In contrast to the case of surface elevations, constrained by the RAMP data, there is no spatially continuous data set that provides a good first estimate for ice thicknesses. The bed elevation model should thus be viewed as a rough hypothesis in regions remote from sites of radar measurements.

[36] Our goal was to interpolate ice thickness values in a way that makes geomorphological sense and that preserves all real features seen in the data, but that avoids manufacturing features for which there is no evidence. We used a five-step process, which is detailed in Appendix B. This process entailed (1) determination of the valley cross-sectional profile from the nearest GPR transects up-glacier and down-glacier; (2) interpolation in regions of sparse data coverage; (3) adjustment of the ice thickness based on surface slope; (4) incorporation of airborne radar data; and (5) incorporation of additional radar data.

[37] Step 1 is to determine the valley cross-sectional profile. We assumed that the form of the valley cross section, normalized in the horizontal direction, is a weighted average of the nearest measured cross sections up and down valley. The closer of these two profiles is weighted more strongly, as a linear function of distance along the valley. For the lower glacier, the horizontal normalization was with respect to the valley width. For the upper glacier (above the mouth of Arena Valley), where the valley is wide and contains a central trough, the normalization was done separately for the central flow band (visible on satellite images) overlying the trough and for either flank.

[38] Step 2 is to interpolate in regions of sparse data coverage. The scheme outlined in step 1 cannot be used for the entire glacier, given its complicated planform geometry. Where the ice is spread out as a broad platform, ice thickness is estimated by linear interpolation between neighboring measured values, or between measured values and the margin. (This applies to the region between the Taylor-Ferrar confluence and Simmons Lower Valley, the region west of Pearse Upper and Simmons Upper Valleys, and the region at the head of Turnabout and Beacon Valleys). For sidelobes, a cross-sectional form was used that interpolates smoothly between all the available spot measurements by GPR. For completeness, we fabricated valley cross sections for Windy Gully and the Cavendish Rocks Icefall, assuming a smooth U-form profile and a maximum ice thickness estimated from the surface slope and a relation for ice flux. We emphasize that none of the quantitative analyses presented in this paper depends on this set of ad hoc assumptions, because our analyses concentrate on locations where direct measurements were sufficiently representative that poorly constrained interpolation was not required.

[39] Step 3 is to adjust the ice thickness based on surface slope. We assumed that the model obtained in step 1, based on linear interpolation, will overestimate (underestimate) the ice thickness where the surface slope is larger (smaller) than the average for that valley segment. It is a well-known property of glaciers that ice thickness ($H$) and surface slope ($\alpha$) vary inversely along a valley, a consequence of the plastic properties of ice. The simplest approach would be to assume a constant value for the product $H\alpha$. But this would certainly lead to variations of $H$ that are too large, because glaciologic stresses do increase where glaciers flow over bedrock highs or down icefalls. Instead we assume that along the glacier centerline, the ice flux proxy $H^5\alpha^3$ varies linearly with distance between measured cross sections where its value is known. This step has little effect on the final model, because our cross-glacier transects are closely spaced on the lower glacier. The rest of the glacier is constrained by longitudinal transects with the airborne radar, described next.

[40] Step 4 is to incorporate airborne radar data. For most of the glacier, excepting the lower 18 km, ice thickness measurements from airborne surveys are available along a longitudinal transect. We used these data to correct the thickness model obtained from step 3. Although this process strongly constrains the result, and increases confidence in its accuracy, it does not mean step 3 is entirely irrelevant; the new model retains a partial imprint of the step 3 model at locations away from the flight path. For example, in some locations the flight path swings close to the valley side, where bedrock slopes are steep. In such places, the mismatches between the measurements and the step 3 model are probably not representative of model errors on the opposite side of the valley. Thus it is useful to retain an imprint of the step 3 model on the valley side away from the flight path.

[41] Step 5 is to incorporate additional radar data. We used additional radar transects, whose orientations with respect to the valley can be considered arbitrary, to make corrections to the model obtained from step 4.

[42] Figure 6b shows the resulting basal elevation model. The most striking feature is the prominent trough beneath the middle upper glacier. Beneath the lower glacier, the valley is a broad, roughly parabolic trough, except where it cuts through the Kukri Hills. Bedrock ridges cross the valley beneath the two prominent icefalls on the upper glacier. All of these features are readily apparent in the ice thickness measurements. The details of their appearance in our model (Figure 6b) should, however, be viewed as no more than plausible inference, except at the locations of direct measurements shown in Figure 5.

## 4. Discussion

### 4.1. Flow

[43] *Robinson* [1984] established that Taylor Glacier flows slowly (typically 5–15 m $a^{-1}$), and that Ferrar Glacier contributes a small quantity of ice to Taylor Glacier at their confluence. Our study confirms these results.

[44] The similarity of flow rates obtained in 1975–1978 and 2002–2004 suggests that Taylor Glacier's flow varies little from year to year. The close agreement between the GPS-derived flow rates and those calculated from radar interferometry in 2000 (Figure 5) further support this conclusion. (Robinson's measurements varied [*Robinson* 1984, Figure 3] but he claimed that only one of the surveys was accurate.) Low interannual variability of velocity is expected for this glacier. It is a thick polar glacier with almost no surface melt; basal lubrication depends on water produced at the bed by geothermal and frictional heating, which should vary little over time. In addition, the glacier lacks other characteristics that would allow rapid changes in

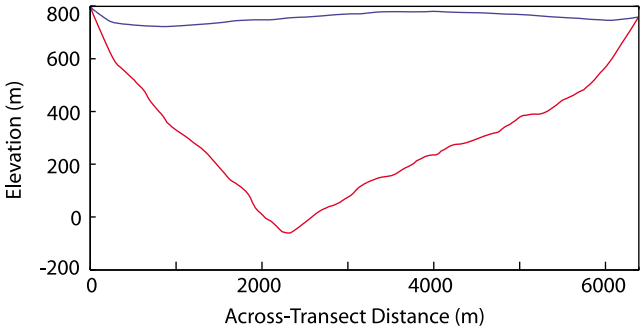


**Figure 7.** Plot of ice surface (blue) and basal (red) elevations across the Taylor-Ferrar confluence, determined from ground-based GPR measurements. Transect trends approximately NE to SW.

flow, such as a floating terminus or active calving front. These characteristics, and the generally slow flow of the glacier, imply that the balance of forces changes only slowly.

[45] Our data show that the ice thicknesses used by Robinson, based on a combination of gravity surveys and along-valley airborne radar transects [*Calkin*, 1974; *Drewry*, 1982], are generally too small. Because the glacier is thicker than previously believed, internal deformation accounts for more of the motion [*Kavanaugh and Cuffey*, 2009].

[46] For much of the middle to upper ablation zone, the flow of Taylor Glacier concentrates in a central filament of relatively fast flowing ice (Figure 3). The filament overlies a bedrock trough, flanked by valley-side benches mantled with thinner ice.

### 4.2. Bed Morphology

[47] The subglacial inset trough (Figure 6b) is a spectacular topographic feature; at one location, it is about 1 km deep and 3 km wide, and thus similar in dimension to Yosemite Valley. How its form varies along the glacier cannot be discerned well from the available data.

[48] The development of an inset trough plausibly reflects two processes. One is a feedback between glacier erosion and ice flux; erosion deepens part of a valley, which then channels the ice flow and concentrates erosion further [*Mazo*, 1987; *Sugden and John*, 1976; *Kessler et al.*, 2008]. Second is that most erosion occurs only if the glacier bed is at melting point, a condition strongly favored by thick ice. As Antarctica cooled in the late Cenozoic, glaciers filling broad valleys in this region would have frozen to their beds on the thin-ice valley flanks before doing so in the valley center. Erosion could thus continue for a longer time in the valley center, accentuating the topographic difference. From visual inspection of adjacent mountain slopes, it appears that the icefalls of the upper glacier overlie dolerite sills; thus lithologic contrasts also might influence the valley form.

[49] Most of the lower part of Taylor Glacier overlies a glacier-wide U-shaped trough, similar in form to the eastern part of Wright Valley and the ice-free lower Taylor Valley. *Hubbard et al.* [2004] mapped the trough beneath the lower 8 km of Taylor Glacier in detail. This is a classic landform of glacial erosion. We note, however, that the subglacial valley cross section is approximately V-shaped at the Taylor-Ferrar confluence (Figure 7). Thus, although a U-shaped cross section is undeniably a typical consequence of glacial erosion, such a shape is not inevitable, even after more than 10 Ma of (probably) frequent glacier occupation. The confluence region likely spent time as a subaerial ridge during glacial lowstands, which would reduce the net erosion by ice. However, the bedrock surface now descends to sea level at its lowest point, so the duration of ice occupation should be similar to that in the adjacent valleys. Currently, only a small flux of ice passes through the confluence [*Kavanaugh et al.*, 2009], a consequence of the similar surface elevations of the glaciers on either side. This situation might be maintained over millions of years, since both glaciers originate from the same flow center.

[50] In a general sense, the morphological form of Taylor Valley (beneath the entire ablation zone of the glacier and eastward into the subaerial section) resembles that of Wright Valley, the ice-free valley trending parallel to Taylor Glacier but on the opposite side of the Asgard Range. The lower (eastern) reaches of both valleys are regular U-shaped troughs. The upper (western) reaches are broad basins with irregular floors. The middle reaches consist of deep troughs inset into highland platforms on the valley flanks and midvalley summits (The Dias in Wright Valley and Pandora Spire and the Friis Hills in Taylor Valley). The general pattern seen in both valleys plausibly reflects a gradient in the degree of glacial scour, with more extensive scour at the low-elevation eastern ends. Despite the fact that total ice discharge should decrease eastward, erosion might increase because the discharge funnels into narrow valleys and because low surface altitude and longitudinally compressive flow both favor melting at the bed.

[51] Landforms in the ice-free valleys have changed little in the last 10 Ma, indicating no major episodes of warm climate in this time [*Denton et al.*, 1993; *Marchant et al.*, 1996]. Currently, sliding contributes little or nothing to the motion of Taylor Glacier [*Kavanaugh and Cuffey*, 2009], indicating that little erosion currently occurs here. This

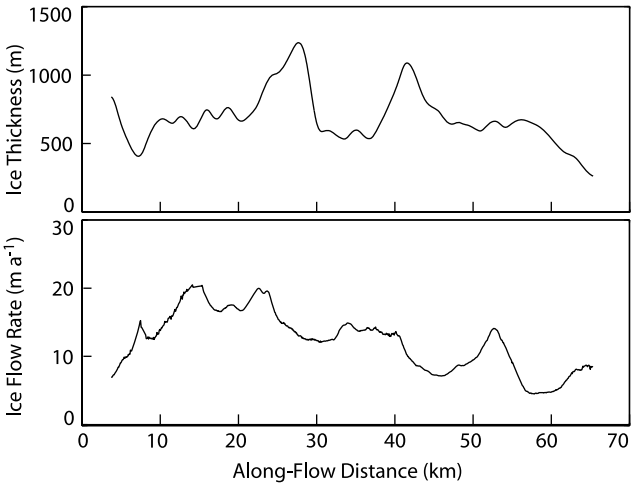


**Figure 8.** Comparison of ice thickness and surface flow rate values along a central flow line of Taylor Glacier. (top) Ice thicknesses estimated using our surface and basal DEMs. (bottom) InSAR-derived surface velocities.

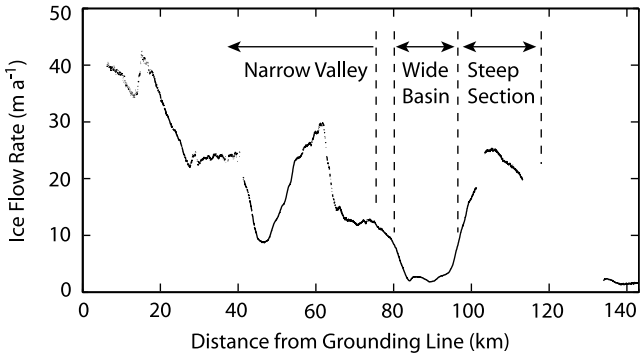


**Figure 9.** Variation of surface velocity for a longitudinal transect of Ferrar Glacier, derived with InSAR. The lower 75 km of the glacier follows a mountain valley with no major variations of width. Above about 80 km, the glacier is much wider.

might suggest that the subglacial form was largely set prior to 10 Ma ago. But the basal temperature in the deep trough is close enough to melting point that minor changes in ice thickness or frictional heating could lead to melting and sliding. A further complicating factor is the possibility of brine layers at the glacier bed, which could permit significant sliding at temperatures below the freezing point of fresh water. A small discharge of salty water emerges at the terminus of Taylor Glacier [*Keys*, 1979]. Radar reflection studies on the lower 6 km of the glaciers identified possible brine layers there [*Hubbard et al.*, 2004], but they are not abundant enough to show in airborne radar [*Holt et al.*, 2006b]. Even in the absence of bulk water or brine at the bed ("bulk" meaning more voluminous than interfacial premelt films), some erosion occurs beneath Dry Valleys glaciers [*Cuffey et al.*, 2000]. The rates are estimated to be extremely low, however, of order $10^{-6}$ m $a^{-1}$.

### 4.3. Cascade and Trickle Models

[52] Neither Taylor Glacier nor Ferrar Glacier resemble the trickle model proposed by *Johnson and Staiger* [2007]. Along Taylor Glacier, velocity varies by about a factor of 2 over kilometer wavelength bed undulations, not by an order of magnitude (Figures 3 and 6b). Nowhere along the central flow line does the velocity fall to a few meters per year or less. Furthermore, deep subglacial basins do not generate peaks in the longitudinal velocity profile (Figure 8). Instead, velocities decrease when the glacier flows into deep basins. Velocity variations are generally associated with bedrock ribs and changes in valley or trough width, as shown in Figures 3, 6, and 8.

[53] These results also apply to Ferrar Glacier. The southeastern corner of Figure 3b shows part of Ferrar Glacier, with relatively slow flow in the deep basin east of the Taylor-Ferrar confluence and fast flow in the thinner ice upstream and downstream. This pattern is opposite to that given by *Johnson and Staiger*'s [2007, Figures 2 and 8] model. Our GPS-measured velocities on Ferrar Glacier indicate flow about 3 times as rapid as predicted by that model, for the same location. We have, in addition, examined the InSAR derived velocities for most of the length of Ferrar Glacier (see Figure 9). Nowhere in the lower 75 km of Ferrar Glacier, the region where it is confined to a narrow valley, do velocities on the centerline fall much below 10 m $a^{-1}$; there are no trickles of order 1 m $a^{-1}$.

[54] The flow of these glaciers is, instead, consistent with the constraints imposed by mass conservation given a slowly varying specific mass balance (and hence a slowly varying flux). It has long been recognized that a glacier flowing by creep conveys a flux proportional to $\alpha^n H^{n+2}$, for an effective surface slope $\alpha$, ice thickness $H$, and stress exponent $n$. ("Effective" slope and ice thickness are center-weighted spatial averages, to account for longitudinal stress gradient coupling [*Kamb and Echelmeyer*, 1986].) Thus, for a constant flux, the driving stress (proportional to $\alpha H$) ought to vary roughly as $H^{-2/n}$. Hence, driving stress reaches its highest values over ridges, not, as Figure 8 of *Johnson and Staiger* [2007] depicts, over subglacial basins. In other words, glaciers move over subglacial ridges by steepening and thickening, but this also causes a thickening and decrease of slope upstream. Our data from Taylor Glacier conform to this classical view of creep flow, if variations of valley width are also considered (the cascade model). Longitudinal stress gradients reduce the sizes of fluctuations but do not change this pattern.

[55] It seems likely that the radar profile of *Calkin* [1974] was a problematic source of information for the trickle model. Such a longitudinal transect cannot be regarded as an accurate model of a valley glacier. Side reflections and wanderings of the flight path lead to large variations of apparent ice thickness that are unrelated to changes in the depth along the central flow line. It is clear from our ice thickness data that Calkin's profile along Taylor Glacier, too, gives a false view of changes in valley depth along the axis of most vigorous flow.

[56] The trickle model is also problematic because it ignores the implications of mass conservation. While a glacier cannot be assumed to be in steady state, the flow and form of most glaciers strongly reflect the steady configuration. For an along-valley section of glacier with no major variations in width, the trickle model thus implies a wholly implausible pattern of dramatic alternation between accumulation and ablation at the glacier surface, or a large departure from the steady form.

## 5. Conclusions

[57] Our new maps of surface velocities and bed and surface elevations provide essential information for analyses of the dynamics and response of the Taylor Glacier system. The system is complex, with a fast flowing stream of ice overlying an inset bedrock trough, flow around large bends, and widely varying bed topography. This situation serves as a natural laboratory for studying the slow flow of cold outlet glaciers through a mountainous landscape. An outlet glacier moving over a rough bed is akin to a cascading river; its surface steepens, and its velocity increases, as it flows over subglacial topographic highs and through valley constrictions. Conversely, its surface flattens and it slows down over subglacial basins.

[58] We have speculated about how the subglacial topography of Taylor Glacier reflects the coevolution of ice flow, glacial erosion, and thermal conditions. This landscape, with its systematic east-west variation and its diversity of

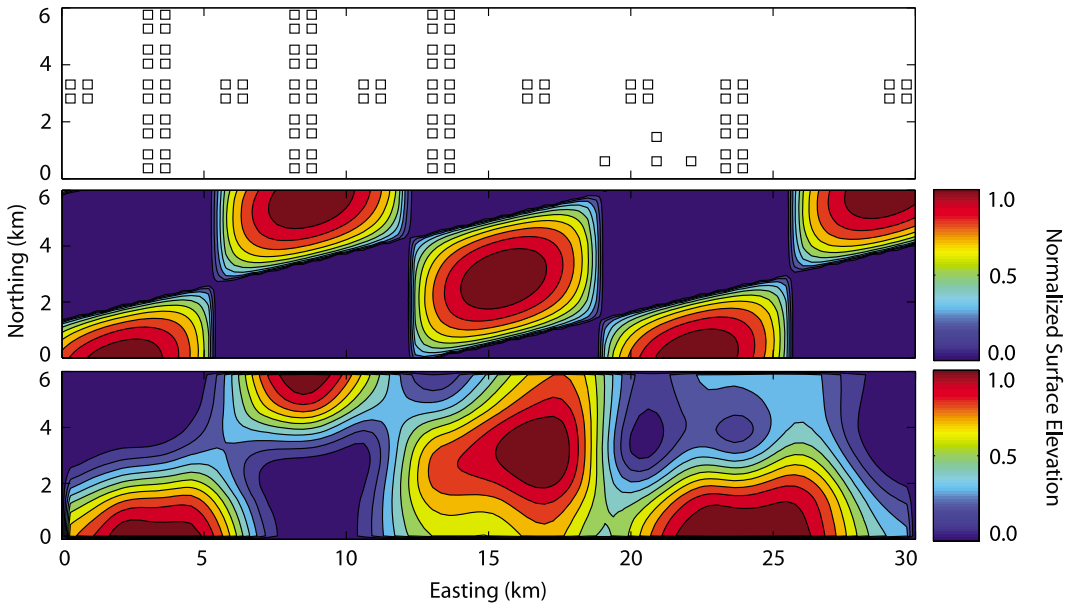


**Figure A1.** (top) A hypothetical "survey grid," with spacing and patterning similar to the Taylor Glacier grid (axes are distances in kilometers). (middle) A "true" offset surface. (bottom) The offset surface estimated from values at survey points, using the interpolation method described in the text. Note the loss of accuracy toward the top right portion of the domain, where the "survey grid" becomes sparse.

forms, might be a useful target for modelers of landscape evolution.

## Appendix A: Surface Elevation Model

[59] Here we provide additional details about the method for constructing the surface elevation model. The final model for surface elevation, $Z$, is

$$Z = Z_R * G_R + \Delta Z_o * G_o, \tag{A1}$$

where $Z_R$ is the RAMP model, $\Delta Z_o$ is the "offset surface," * denotes convolution, and $G_R$ and $G_o$ are filter functions. The purpose of the offset surface is to warp the elevation model to match values measured by GPS. The filters are symmetrical, two-dimensional, center-weighted (parabolic) functions, with specified radii. For $G_R$, the radius is $2 \cdot \max(H_o, H)$, with $H_o$ = 400 m; thus the radius is 800 m where the ice is thin, but $2H$ otherwise. For $G_o$, the radius is 1 km.

[60] The method we used for calculating the value of the "offset surface" at any arbitrary coordinate ($\vec{X}$) in the elevation model is as follows. First, it is necessary to specify the number of survey sites used. We define two numbers, $N_{\min}$ and $N_{\max}$, to be the minimum and maximum possible number of sites used. Next, we determine the distances $\chi_j$ between $\vec{X}$ and the $N_{\max}$ closest sites ($j = 1 \cdots N_{\max}$). The closest site is distance $\chi_1$ from the coordinate $\vec{X}$. We then define the number of sites used ($N_s$) as

$$N_s = N_{\min} + \left\lfloor (N_{\max} - N_{\min}) \operatorname{erf}\left(\frac{\chi_1}{L_1}\right) \right\rfloor, \tag{A2}$$

where $L_1$ is a specified length scale, and $\lfloor F \rfloor$ means round $F$ down to the nearest integer. Equation (A2) specifies that a smaller number of survey sites are used at coordinates $\vec{X}$ near to survey sites than at coordinates far from any survey sites. By applying equation (A2), at least $N_{\min}$ survey sites are always used, in order to average out errors, but the number of sites does not exceed a cap.

[61] Each site $i = 1 \cdots N_s$ is then assigned a weight $\omega_i$ according to

$$\omega_i = \exp\left[-\left[\frac{\chi_1}{L_2} + \left(\frac{\chi_i}{\chi_1} - 1\right)\right]\right], \tag{A3}$$

where $L_2$ is another specified length scale. If we call the measured discrepancy between RAMP and GPS elevations at each site $\Delta z_i$, then the offset surface is

$$\Delta Z_o(\vec{X}) = \frac{\sum_i \omega_i \Delta z_i}{\sum_i \omega_i}. \tag{A4}$$

Equations (A3) and (A4) specify that the closest survey sites to $\vec{X}$ are given the greatest weight, and that any group of survey sites at approximately the same distance from $\vec{X}$ will be assigned approximately the same weights.

[62] We used parameter values $N_{\min} = 4$, $N_{\max} = 8$, $L_1 = 1.5$ km, and $L_2 = 2$ km. The final $Z$ is not sensitive to parameter values within reasonable ranges. Within clusters, the distances between survey sites is about 0.5 km. Most locations on the glacier are within a few kilometers of some survey sites. Hence a "reasonable range" for the length scales is 1–3 km. Choosing $N_{\min} = 4$ reflects the clustering of survey sites into groups of four. The value $N_{\max} = 8$ is more arbitrary but means that a coordinate located between two of the four-pole clusters, but not close to either one, will be influenced by all sites in both clusters.

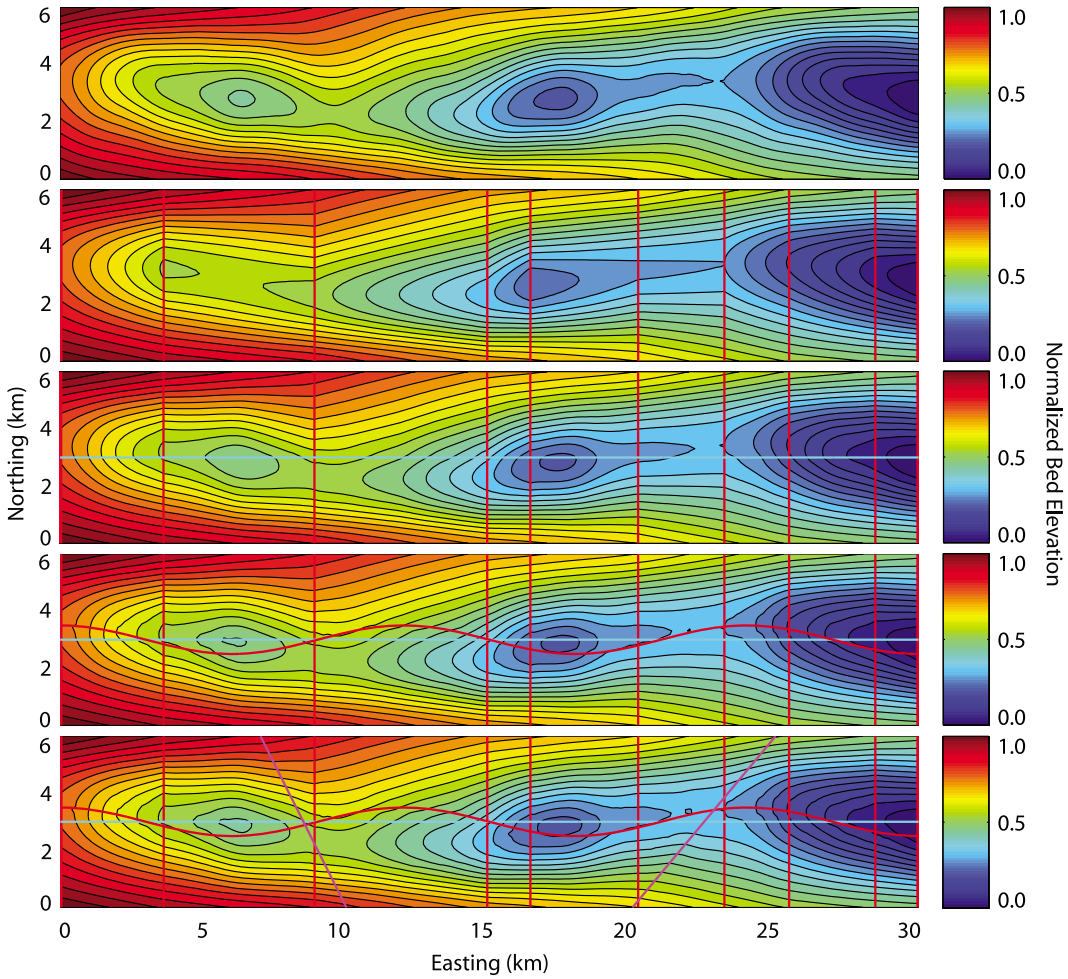


**Figure B1.** (first panel) Hypothetical "true" basal elevations along a glacier. (second panel) Suppose cross-glacier ground-based radar transects are obtained along the vertical red lines; (third panel) ice thicknesses are adjusted based on ice thickness and surface slope values along the blue centerline; (fourth panel) an airborne radar transect is obtained along the red meandering curve; and (fifth panel) additional airborne transects are obtained along the purple lines. In sequence, the second to fifth panels represent elevation models resulting from steps 1, 3, 4, and 5 as described in the text.

[63] Figure A1 illustrates how the method performs for a hypothetical case with a known answer and a density of survey sites that varies from good to poor.

## Appendix B: Basal Elevation Model

[64] Here we provide additional details about the method for constructing the basal elevation model, with reference to the five-step process outlined in the text. Figure B1 illustrates how the method performs for a hypothetical case with a known answer.

### B1. Step 1: Determination of the Valley Cross-Sectional Profile

[65] For the initial interpolation between cross-glacier transects, the following process was used. (1) To simplify calculations, we projected the ice thickness values for each transect onto a line determined by a least squares fit to the Easting and Northing coordinates of that transect. (2) Ice thickness values between transect endpoints and the glacier margins were assumed to decrease linearly to zero. Thus, we do not attempt to resolve marginal cliffs, which are small compared to the large-scale features of the glacier studied here. As noted above, surface elevations are also poorly constrained in these regions. (3) Basal elevation values were subsampled at 201 evenly spaced nodes along the transect; this simplifies the interpolation between adjacent transects performed in step 7. (4) Ice thickness values were subtracted from elevation values interpolated from the 200 m surface DEM to obtain basal elevations at these points along the transect. (5) The along-margin distance between transects was then calculated at each glacier margin, and a series of $J$ intermediate transects was generated at evenly spaced intervals between the GPR transect lines. These intermediate transects were spaced no greater than 25 m apart. (6) The widths of the two GPR transects were normalized to 1. (7) For each intermediate transect $j = 1, 2, 3, \ldots, J$ (here numbers increase with distance up glacier), basal

elevation $z_B(i)$ was determined at each of the 201 nodes $i$ by

$$z_B(i) = z_{B1}(i) + \frac{j}{J+1}[z_{B2}(i) - z_{B1}(i)]. \quad \text{(B1)}$$

Here $z_{B1}(i)$ and $z_{B2}(i)$ are the basal elevation values at the $i$th node of GPR transects 1 (the down-glacier transect) and 2 (the up-glacier transect), respectively. (8) The resulting basal elevation values were projected onto the appropriate Easting and Northing coordinates along the intermediate transects.

[66] Although this interpolation scheme is more complex than nearest-neighbor algorithms, it has the benefit of preserving morphological characteristics of the measured cross sections. It also yields an interpolation of basal elevations that is linear with respect to the along-margin distance between measured transects, a property desirable for its simplicity.

### B2. Step 2: Interpolation in Regions of Sparse Data Coverage

[67] At the terminus and at sidelobes, the ice thickness was varied linearly from the margin (where it is zero) to the nearest location of measurements.

[68] For the Cavendish Rocks Icefall and for Windy Gully, steep and crevassed ice made direct GPR measurements untenable. Instead, we roughly estimated the ice thickness based on the measured fluxes through the flow bands emanating from these features. The approach uses the nominal ice flux relation for a glacier flowing by internal deformation; for an exponent of $n = 3$ in Glen's flow law, the ice flux $q$ is nominally related to the ice thickness $H$ and surface slope $\alpha$ by $q \propto H^5\alpha^3$.

[69] We first estimated the ice flux through the Cavendish Rocks Icefall from measurements of velocity and thickness where our transect T09 crosses the flow band at the foot of the icefall (there is a clear topographical "suture" where the ice passing through the icefall rejoins the main flow). The flux was calculated as

$$q = 0.855 \int_0^W v(w)H(w)\mathrm{d}w, \quad \text{(B2)}$$

where $w$ is distance across flow and $W$ is total width of the flow band. An effective ice thickness $H_e$ was then defined as

$$H_e = \left(\frac{q}{W\alpha^3}\right)^{\frac{1}{5}}. \quad \text{(B3)}$$

In addition, a constant $C_H$ was defined to specify a relation $H_{\max} = C_H H_e$, where $H_{\max}$ denotes the ice thickness at the point of maximum velocity along the measured transect. Values for $\alpha$ and $W$ for the icefall itself were applied, together with the estimated $q$ from equation (B2), to calculate $H_e$ for the icefall. The maximum thickness in the icefall was then calculated from $C_H$. This maximum ice thickness value was then used to scale an assumed cross-sectional profile shape, a nominal "smooth U-shaped cross section." The shape was constructed using, as a model, the most uniform and U-shaped profile we measured (a cross section of the lower glacier, between transects T03 and T06). This measured profile was averaged with its own mirror image to form a symmetric profile.

[70] A similar procedure was used to determine the cross-sectional profile for Windy Gully. In this case the flux $q$ was estimated from where the Windy Gully flow band crosses our transect T12. Here the suture of Windy Gully and Taylor Glacier ice is marked by a medial moraine.

### B3. Step 3: Ice Thickness Adjustment Based on Surface Slope

[71] At each point where the centerline intersects a cross-valley GPR transect, we calculated the variable $\eta_{CL} = H_0^5\alpha^3$ assuming that between these points, $\eta$ along the centerline ($\eta_{CL}$) varies linearly with distance $d_{CL}$. The scaling factor $\xi$ was then calculated along the centerline as

$$\xi(d) = \frac{1}{H_0(d_{CL})}\left(\frac{\eta(d_{CL})}{\alpha(d_{CL})^3}\right)^{1/5}. \quad \text{(B4)}$$

For each point $\vec{X}$ on the glacier surface, two distances were calculated: $A$, the perpendicular distance to the nearest ground-based GPR transect, and $B$, the distance to the nearest point on the centerline. Then the new thickness model ($H_3$, with subscript 3 indicating the model obtained in the third step) was calculated from the previous model ($H_1$) at all points by $H_3(\vec{X}) = \gamma H_1(\vec{X})$, with

$$\gamma(\vec{X}) = \xi^\dagger \frac{A}{A+B} + \frac{B}{A+B}; \quad \text{(B5)}$$

and with $\xi^\dagger = \xi(d_{CL}^\dagger)$ the value of $\xi$ at the nearest centerline point. This relationship has the following properties: (1) where $\xi = 1$, $\gamma = 1$ for all values of $A$ and $B$; (2) where $A = 0$, $\gamma = 1$ for all values of $\gamma$ and $B$; and (3) where $B = 0$, $\gamma = \xi$. By property 2, ice thickness values are unchanged in locations where GPR soundings have been made, and by property 3 the full correction factor $\xi$ is applied only along the prescribed centerline.

### B4. Step 4: Incorporation of Airborne Radar Data

[72] This step incorporates the longitudinal transect of GPR measurements shown in Figure 2 (magenta curve along glacier center). Along each point $d_{FL}$ of this flight path, we defined $\zeta = H_{FL}/H_3$; this is the dimensionless factor by which the ice thickness model $H_3$ must be multiplied to match the measurement at that location. For each point $\vec{X}$ on the glacier surface, we then calculated the new ice thickness value $H_4$ as $H_4(\vec{X}) = \hat{\gamma}H_3(\vec{X})$, where the scaling factor $\hat{\gamma}$ is

$$\hat{\gamma}(\vec{X}) = \zeta\left(d_{FL}^\dagger\right)\frac{A}{A+C} + \frac{C}{A+C}. \quad \text{(B6)}$$

Here $A$ is defined as above and $C$ is the distance to the nearest flight line point $d_{FL}^\dagger$. This relationship is similar to equation (B5) and thus has similar properties ($\hat{\gamma} = 1$ where $\zeta = 1$ and/or $A = 0$; $\hat{\gamma} = \zeta$ where $C = 0$). So defined, ice thickness values are unchanged at locations where

measured thickness values match the previous thickness model $H_3$; along the flight path, as at ground-based transects, the new model matches the measurements exactly.

### B5. Step 5: Incorporation of Additional Radar Data

[73] This step was used to incorporate ice thickness measurements along the additional magenta curves in Figure 2, and is intended to apply only to a local area surrounding the locations of each new measurement $H_+$. The method described here can be applied to any future measurements placed arbitrarily on the glacier. First, we calculated the difference between the new measured values and the old model $\Delta H_+ = H_+ - H_4$. For each point $\vec{X}$ on the glacier surface, we performed the following operations:

[74] 1. Values for $D$, the distance to the closest point ($d_+$) along the new transect, and $I$, which is the smaller of values $A$ and $C$, defined above (i.e., the closest distance to a prior measurement), were determined.

[75] 2. At $d_+$, we examined the value of $\Delta H_+$ and defined $\delta_0$ as

$$\delta_0(\vec{X}) = \Delta H_+(d_+) \qquad \text{if} \quad \Delta H_+ > 0 \tag{B7}$$

$$\delta_0(\vec{X}) = H_2(\vec{X})\frac{\Delta H_+(d_+)}{H_4(d_+)} \qquad \text{if} \quad \Delta H_+ \le 0, \tag{B8}$$

where $H_4(d_+)$ is the old modeled thickness value at the point $d_+$ (which has a new measured thickness). This definition for $\delta_0$ ensures that the ice thickness in deep regions adjacent to the flight path will not increase dramatically, and also ensures that negative ice thicknesses will not be calculated in regions of thin ice.

[76] 3. To ensure that adjustments were applied only to a region near the new data, the magnitude of the ice thickness correction was specified to diminish as a Gaussian function with a length scale $\lambda_1$ = 5 km:

$$\delta_1 = \delta_0 \exp\left[-\left(\frac{D}{\lambda_1}\right)^2\right]. \tag{B9}$$

[77] 4. The correction must also be zero at the locations of prior measurements. The term $\delta_2$ was defined such that

$$\delta_2 = \delta_1 \frac{I}{D+I}. \tag{B10}$$

This equals zero at sites of prior measurements ($I = 0$), and equals $\delta_1$ at sites of new measurements ($D = 0$).

[78] 5. Small-wavelength undulations revealed by the measurements are not likely to reflect widespread topographic features. Thus it is best to apply only a smoothed version of the correction $\delta_2$. We calculated a new function $\delta_3$ by convolving $\delta_2$ with a filter (here a conical filter of length scale 3 km). This smoothed surface does not match values at measured transects; to restore the agreement with measurements, we calculated a final correction $\delta_4$, linear combination of the unsmoothed and smoothed functions:

$$\delta_4 = f\delta_2 + (1-f)\delta_3. \tag{B11}$$

The weighting factor $f$ is defined as a Gaussian function of $M$, the minimum distance to any site where measurements were obtained (new or old). We used a length scale of 1 km for this Gaussian. At distance $M = 0$, $f = 1$, and the unsmoothed correction $\delta_2$ is applied. As $M$ increases, $f \to 0$, and $\delta_4$ increasingly resembles the spatially averaged version $\delta_3$.

[79] The final ice thickness model is $H = H_4 + \delta_4$. Figure B1 illustrates the entire process.

[80] **Acknowledgments.** This work was funded by the U.S. National Science Foundation, grants OPP-0125579 to K.C. and OPP-0126202 to D.M. We gratefully acknowledge additional support from the Hellman Family Faculty Fund to University of California, Berkeley. We thank A. Fountain, T. Nylen, and H. Basagic of Portland State University for valuable contributions over the last 5 years; the personnel of the Byrd Field Center and Petroleum Helicopters Inc.; and colleagues at the University of Texas Institute for Geophysics who run the aerogeophysics program. We are grateful to A. Bliss, S. Aciego, and J. Sanders for their assistance in the field and to the anonymous reviewers and Associate Editor for their constructive and thoughtful comments.

## References

Aciego, S. M., K. M. Cuffey, J. L. Kavanaugh, D. L. Morse, and J. P. Severinghaus (2007), Pleistocene ice and paleo-strain rates at Taylor Glacier, Antarctica, *Quat. Res.*, *68*, 303–313, doi:10.1016/j.yqres.2007.07.013.

Brook, E. J., M. D. Kurz, R. P. Ackert Jr., G. H. Denton, E. T. Brown, G. M. Raisbeck, and F. Yiou (1993), Chronology of Taylor Glacier advances in Arena Valley, Antarctica, using in-situ cosmogenic $^3$He and $^{10}$Be, *Quat. Res.*, *39*, 11–23, doi:10.1006/qres.1993.1002.

Calkin, P. E. (1974), Subglacial geomorphology surrounding the ice-free valleys of southern Victoria Land, Antarctica, *J. Glaciol.*, *13*, 415–429.

Cuffey, K. M., H. Conway, A. M. Gades, B. Hallet, R. Lorrain, J. P. Severinghaus, E. J. Steig, B. Vaughn, and J. W. C. White (2000), Entrainment at cold glacier beds, *Geology*, *28*, 351–354, doi:10.1130/0091-7613(2000)28<351:EACGB>2.0.CO;2.

Cuffey, K. M., A. Bliss, and J. Kavanaugh (2007), Surface velocities of Taylor Glacier, Antarctica, digital media, Natl. Snow and Ice Data Cent., Boulder, Colo.

Denton, G. H., J. G. Bockheim, S. C. Wilson, and M. Stuiver (1989), Late Wisconsin and early Holocene glacial history, inner Ross Embayment, Antarctica, *Quat. Res.*, *31*, 151–182, doi:10.1016/0033-5894(89)90004-5.

Denton, G. H., D. E. Sugden, D. R. Marchant, B. L. Hall, and T. I. Wilch (1993), East Antarctic Ice Sheet sensitivity to Pliocene climatic change from a dry valleys perspective, *Geogr. Ann., Ser. A*, *75*, 155–204, doi:10.2307/521200.

Doran, P. T., et al. (2002), Antarctic climate cooling and terrestrial ecosystem response, *Nature*, *415*, 517–520, doi:10.1038/nature710.

Drewry, D. J. (1982), Ice flow, bedrock, and geothermal studies from radio echo sounding inland of McMurdo Sound, Antarctica, in *Antarctic Geoscience 1*, edited by C. Craddock, pp. 977–983, Univ. of Wisc. Press, Madison.

Fountain, A. G., et al. (1999), Physical controls on the Taylor Valley ecosystem, Antarctica, *BioScience*, *49*, 961–971, doi:10.2307/1313730.

Gades, A. M. (1998), Spatial and temporal variations of basal conditions beneath glaciers and ice sheets inferred from radio echo soundings, Ph.D. thesis, Univ. of Wash., Seattle.

Grootes, P. M., E. J. Steig, M. Stuiver, E. D. Waddington, and D. L. Morse (2001), The Taylor dome antarctic $^{18}$O record and globally synchronous changes in climate, *Quat. Res.*, *56*, 289–298, doi:10.1006/qres.2001.2276.

Hendy, C. H., T. R. Healy, E. M. Rayner, J. Shaw, and A. T. Wilson (1979), Late Pleistocene glacial chronology of the Taylor Valley, Antarctica, and the global climate, *Quat. Res.*, *11*, 172–184, doi:10.1016/0033-5894(79)90002-4.

Higgins, S. M., C. H. Hendy, and G. H. Denton (2000), Geochronology of Bonney Drift, Taylor Valley, Antarctica: Evidence for interglacial expansions of Taylor Glacier, *Geogr. Ann., Ser. A*, *82*, 391–409, doi:10.1111/1468-0459.00130.

Holt, J. W., M. E. Peters, S. D. Kempf, D. L. Morse, and D. D. Blankenship (2006a), Echo source discrimination in single-pass airborne radar sounding data from the Dry Valleys, Antarctica: implications for orbital sounding of Mars, *J. Geophys. Res.*, *111*, E06S24, doi:10.1029/2005JE002525.

Holt, J. W., M. E. Peters, D. L. Morse, D. D. Blankenship, L. E. Lindzey, J. L. Kavanaugh, and K. M. Cuffey (2006b), Identifying and characteriz-

ing subsurface echoes in airborne radar sounding data from a high-clutter environment, paper presented at Eleventh International Conference on Ground Penetrating Radar, Ohio State Univ., Columbus, Ohio, 19–22 June.

Hubbard, A., W. Lawson, B. Anderson, B. Hubbard, and H. Blatter (2004), Evidence for subglacial ponding across Taylor Glacier, Dry Valleys, Antarctica, *Ann. Glaciol.*, *39*, 79–84, doi:10.3189/172756404781813970.

Johnson, J. V., and J. W. Staiger (2007), Modeling long-term stability of the Ferrar Glacier, East Antarctica: Implications for interpreting cosmogenic nuclide inheritance, *J. Geophys. Res.*, *112*, F03S30, doi:10.1029/2006JF000599.

Kamb, B., and K. Echelmeyer (1986), Stress-gradient coupling in glacier flow: 1. Longitudinal averaging of the influence of ice thickness and surface slope, *J. Glaciol.*, *32*, 267–284.

Kavanaugh, J. L., and K. M. Cuffey (2009), Dynamics and mass balance of Taylor Glacier, Antarctica: 2. Force balance and longitudinal coupling, *J. Geophys. Res.*, *114*, F04011, doi:10.1029/2009JF001329.

Kavanaugh, J. L., K. M. Cuffey, D. L. Morse, A. K. Bliss, and S. M. Aciego (2009), Dynamics and mass balance of Taylor Glacier, Antarctica: 3. State of mass balance, *J. Geophys. Res.*, *114*, F04012, doi:10.1029/2009JF001331.

Kessler, M. A., R. S. Anderson, and J. P. Briner (2008), Fjord insertion into continental margins driven by topographic steering of ice, *Nat. Geosci.*, *1*, 365–369, doi:10.1038/ngeo201.

Keys, J. R. (1979), Saline discharge at the terminus of Taylor Glacier, *Antarct. J. U. S.*, *14*(5), 82–85.

Liu, H., K. Jezek, B. Li, and Z. Zhao (2001), Radarsat Antarctic Mapping Project digital elevation model version 2, digital media, Natl. Snow and Ice Data Cent., Boulder, Colo.

Lyons, W. B., A. Fountain, P. Doran, J. C. Priscu, K. Neumann, and K. A. Welch (2000), Importance of landscape position and legacy: The evolution of the lakes in Taylor Valley, Antarctica, *Freshwater Biol.*, *43*, 355–367, doi:10.1046/j.1365-2427.2000.00513.x.

Marchant, D. R., G. H. Denton, and C. C. Swisher III (1993), Miocene-Pliocene-Pleistocene glacial history of Arena Valley, Quartermain Mountains, Antarctica, *Geogr. Ann., Ser. A*, *75*, 269–302, doi:10.2307/521204.

Marchant, D. R., G. H. Denton, C. C. Swisher, and N. Potter (1996), Late Cenozoic Antarctic paleoclimate reconstructed from volcanic ashes in the dry valleys region of southern Victoria Land, *Geol. Soc. Am. Bull.*, *108*, 181–194, doi:10.1130/0016-7606(1996)108<0181:LCAPRF>2.3.CO;2.

Mazo, V. L. (1987), Effects of glacial erosion on the flow of ice sheets and the morphology of their beds, *IAHS Publ.*, *170*, 145–155.

Monnin, E., et al. (2004), Evidence for substantial accumulation rate variability in Antarctica during the Holocene, through synchronization of $CO_2$ in the Taylor Dome, Dome C, and DML ice cores, *Earth Planet. Sci. Lett.*, *224*, 45–54, doi:10.1016/j.epsl.2004.05.007.

Morse, D. L., E. D. Waddington, and E. J. Steig (1998), Ice age storm trajectories inferred from radar stratigraphy at Taylor Dome, Antarctica, *Geophys. Res. Lett.*, *25*, 3383–3386, doi:10.1029/98GL52486.

Morse, D. L., E. D. Waddington, H.-P. Marshall, T. A. Neumann, E. J. Steig, J. E. Dibb, D. P. Winebrenner, and R. J. Arthern (1999), Accumulation rate measurements at Taylor Dome, East Antarctica: Techniques and strategies for mass balance measurements in polar environments, *Geogr. Ann., Ser. A*, *81*, 683–694, doi:10.1111/j.0435-3676.1999.00096.x.

Morse, D. L., E. D. Waddington, and L. A. Rasmussen (2007), Ice deformation in the vicinity of the ice-core site at Taylor Dome, Antarctica, and a derived accumulation history, *J. Glaciol.*, *53*(182), 449–460, doi:10.3189/002214307783258530.

Paterson, W. S. B. (1994), *The Physics of Glaciers*, 3rd ed., 480 pp., Elsevier Sci., Tarrytown, N. Y.

Peters, M. E., D. D. Blankenship, and D. L. Morse (2005), Analysis techniques for coherent airborne radar sounding: Application to West Antarctic ice streams, *J. Geophys. Res.*, *110*, B06303, doi:10.1029/2004JB003222.

Robinson, P. H. (1984), Ice dynamics and thermal regime of Taylor Glacier, South Victoria Land, Antarctica, *J. Glaciol.*, *30*(105), 153–160.

Steig, E. J., et al. (2000), Wisconsinan and Holocene climate history from an ice core at Taylor Dome, western Ross Embayment, Antarctica, *Geogr. Ann., Ser. A*, *82*, 213–235, doi:10.1111/1468-0459.00122.

Sugden, D. E., and B. S. John (1976), *Glaciers and Landscape*, 376 pp., Edward Arnold, London.

H. Conway, Department of Earth and Space Sciences, University of Washington, Box 351310, Seattle, WA 98195, USA. (conway@ess.washington.edu)

K. M. Cuffey, Department of Geography, University of California, 507 McCone Hall, Berkeley, CA 94720-4740, USA. (kcuffey@berkeley.edu)

J. L. Kavanaugh, Department of Earth and Atmospheric Sciences, University of Alberta, 1-26 Earth Sciences Building, Edmonton, AB T6G 2E3, Canada. (jeff.kavanaugh@ualberta.ca)

D. L. Morse, Institute for Geophysics, University of Texas at Austin, 10100 Burnet Road, Building 196, Austin, TX 78758, USA.

E. Rignot, Department of Earth System Science, University of California, Croul Hall, Irvine, CA 92697, USA. (erignot@uci.edu)